Numerical Modelling of Waterhammer Pressure Pulse Propagation in Sand Reservoirs

Mahshid Jafar Pour[1,], Alireza Nouri, Dave Chan

University of Alberta, Edmonton, Alberta, Canada

Abstract

This paper presents a numerical model with a new approach for analyzing the propagation of pressure waves in porous media and investigates the dynamic response of sand in relation to the attributes of pore pressure pulses. There are various instances in which dynamic phenomena can have a significant impact on porous media in a reservoir. One notable example is the possible influence of waterhammer pressure pulsing on sand fluidization around injection wells in oil reservoirs following a hard wellbore shut-in, which can result in massive sand production. In some extreme cases, this phenomenon can even result in the loss of the wellbore. Nevertheless, the pore pressure wave propagation in porous media has often been neglected in modeling likely due to mathematical complexity.

The proposed model solves the momentum balance of fluid and solid coupled with the fluid mass balance equation in the prediction of dynamic fluid flow and mechanical deformation in porous media. The model is a two-dimensional, elasto-plastic, axisymmetric, single-phase and sequentially coupled model. The numerical model was validated against experimental data for a step wave in a shock tube and good agreement between model calculations and measured data has been obtained.

Two distinct waves have been observed as a result of a shock pore pressure wave. The first one is an undrained wave where fluid and solid travel at the same speed. The other one is a wave which is often damped far from the source due to the friction between fluid and solid as they no longer travel together. It is found that tortuosity plays an important role on the amplitude of the waves. The results were then compared to the predictions

[1] *Email address:* mashid@ualberta.ca; *Tel:* +1-780-492-4117

by Biot's theory for waves through porous media. Biot's theory is shown to be inaccurate in predicting the transient dynamic behaviour, but it is sufficient in capturing the overall trends. Finally, the model is used to predict waterhammer response in near wellbore reservoir.

1. Introduction

Coupling of fluid flow with geomechanics is necessary when analysing the propagation of pore pressure waves in porous media. Biot (1941) proposed the theory of poroelasticity which ignores the acceleration terms and wave effects. By wave we mean any discontinuity or jump in the field parameters such as pressure, temperature and stress (Hill. 1962). Later, Biot extended his formulations to elastic waves in saturated porous media for low frequency (Biot, 1956a) and high frequency waves (Biot, 1956b). A wave with low frequency is defined as the wave whose wavelength is less than the pore scale for which Poiseuille flow is valid (Sivrikoz, 2009). Different mathematical modeling is required at high frequencies since certain parameters such as permeability and tortuosity are frequency dependent. Biot's formulations have been used extensively in various applications including the study of the effects of earthquake shear waves on saturated sand response (Cheng, 1986; Desai and Galagoda, 1989) to the ultrasonic waves travelling in human bones (Lakes et al., 1986). The applications however focus on stress waves and ignore the effect of pore pressure waves in the fluid flow mainly because they are mostly damped and are of importance only around the source. Another reason is that Biot's theory predicts two waves in porous media while the second wave was not observed experimentally in porous media until 1980 (Plona, 1980) and later by Van der Grinten et al. (1985) in soil. An example of pore pressure wave is waterhammer (WH) waves around an injector wellbore, the effects of which can be detrimental to the stability of wellbore and is suspected to induce sudden massive sand production because of sand liquefaction (Santarelli et al., 2000; Hayatdavoudi, 2005; Santarelli et al., 2011). The exposure of the reservoir to water hammer amplitudes that can move the stress conditions towards near-zero mean effective stress (or liquefaction conditions) poses a potential risk to the stability of the wellbore.

Verruijt (2010) presented an analytical solution using Biot's 1D dynamic

formulation for a shock pore pressure wave and showed that two p-waves are generated as a result of a shock wave. He also verified the results with numerical simulations and obtained a reasonable match. The simulation results, however, showed numerical oscillations when shock waves were calculated.

De la Cruz and Spanos (1989) solved the thermodynamics of porous media for low-frequency seismic waves. They used continuity and momentum balance equations and added thermal coupling to the poroelasticity equations and treated porosity as a primary variable. In their formulation, they related velocities and deformations to heat generation of the second order and compression to heat generation of the first order. They showed that the heat flow leads to wave attenuation. Their formulation has been used in the mathematical demonstration of the feasibility of the application of pore pressure pulsing as an Enhanced Oil Recovery (EOR) method (Spanos et al., 1999).

Sivrikoz (2009) simplified the equations presented by de la Cruz and Spanos (1989) for pore pressure and solid displacements as the main variables under isothermal conditions, and solved them for the application of pressure pulsing as an EOR method. The method of solution adopts an elastic constitutive model to simplify the governing equations and is not applicable to elasto-plastic cases.

The work presented in this paper adopted the approach proposed by de la Cruz and Spanos (1989) for a saturated porous medium, ignoring the thermal effects by assuming isothermal conditions, assuming 2D axial symmetry, and employing artificial viscosity to damp the numerically-induced oscillations and achieve smooth response for shock waves. An elasto-plastic constitutive model was implemented to account for inelastic deformations. The state variables were chosen to be fluid velocity, solid velocity, pore pressure, porosity and stresses. The model was validated against experimental data published by van der Grinten et al. (1985) and van der Grinten et al. (1987). The results were also compared with those of Biot's formulation. The explicit finite difference method was used to solve the governing equations by employing a sequential coupling scheme combined with the velocity-stress method (Virieux. 1986).

2. Theory and Background

De la Cruz and Spanos (1989) derived the governing equations for elastic solids by substituting stresses with displacements in Hook's law. The

following equations are derived for isothermal conditions.

2.1. Mass Balance Equation for Elastic Medium

The derivation of mass balance is expressed in more details to emphasize the assumption of elasticity in describing the solid response. Next section will discuss changes required on the governing equations for a more general constitutive model for solid. The mass balance equation for fluid is:

$$\frac{\partial(n\rho_f)}{\partial t} + Div(n\rho_f \boldsymbol{v}) = 0 \tag{1}$$

where n is the porosity, ρ_f is the fluid density and $\boldsymbol{v}$ is the fluid velocity vector. This equation is Eulerian while the solid momentum equation is usually expressed in the Lagrangian framework. Due to solid deformation, the change in mass will not be equal to the change in $n\rho_f$. Hence, the material derivative is introduced:

$$\frac{\partial()}{\partial t} = \frac{d()}{dt} - \boldsymbol{w}.Grad() \tag{2}$$

where $\boldsymbol{w}$ is solid velocity vector. The mass balance equation for the fluid can be rewritten as:

$$\frac{d(n\rho_f)}{dt} - \boldsymbol{w}.Grad(n\rho_f) + Div(n\rho_f \boldsymbol{v}) = 0 \tag{3}$$

Also since divergence is a linear operator, it satisfies the product rule. Therefore, for any vector $\boldsymbol{F}$ and scalar a, one can write:

$$Div(a.\boldsymbol{F}) = Grad(a).\boldsymbol{F} + aDiv(\boldsymbol{F}) \tag{4}$$

Now if $a = n\rho_f$ and $\boldsymbol{F} = \boldsymbol{w}$, it yields:

$$\boldsymbol{w}.Grad(n\rho_f) = Div(n\rho_f \boldsymbol{w}) - n\rho_f Div(\boldsymbol{w}) \tag{5}$$

Replacing $\boldsymbol{w}.Grad(n\rho_f)$ in the mass balance equation:

$$\frac{d(n\rho_f)}{dt} + n\rho_f Div(\boldsymbol{w}) + Div(n_f(\boldsymbol{v} - \boldsymbol{w})) = 0 \tag{6}$$

Fluid compressibility is defined as:

$$C_f = \frac{\partial \rho_f}{\rho_f \partial p_T} = \left(\frac{\frac{\partial \rho_f}{\partial t}}{\rho_f(\partial p/\partial t)}\right)_T \tag{7}$$

4

under isothermal conditions:

$$\frac{d(n\rho_f)}{dt} = (n\frac{d\rho_f}{dp}\frac{dp}{dt} + \rho_f\frac{dn}{dt}) = (n\rho_f C_f\frac{dp}{dt} + \rho_f\frac{dn}{dt}) \qquad (8)$$

The porosity change proposed here depends on the solid and fluid compressibilities and is valid only for elastic behavior:

$$\frac{d(n)}{dt} = (\alpha - n)C_s\frac{dp}{dt} + (\alpha - n)Div(\boldsymbol{w}) \qquad (9)$$

where C_s is the grain compressibility and α is the Biot's coefficient. Elastoplastic deformations are discussed in the next section. Substituting Eq. 9 in Eq. 6 one obtains:

$$\rho_f(nC_f + (\alpha - n)C_s)\frac{dp}{dt} + \rho_f\alpha Div(\boldsymbol{w}) + Div(n\rho_f(\boldsymbol{v} - \boldsymbol{w})) = 0 \qquad (10)$$

Defining storativity as: $S_p = nC_f + (\alpha - n)C_s$, the mass balance equations yields:

$$S_p\frac{dp}{dt} + \alpha Div(\boldsymbol{w}) + \frac{1}{\rho_f}Div(n\rho_f(\boldsymbol{v} - \boldsymbol{w}))) = 0 \qquad (11)$$

Verruijt (2010) derived the same equation by combining solid and fluid mass balance equations. Using Eq. 4 one obtains:

$$Div(n\rho_f(\boldsymbol{v} - \boldsymbol{w})) = (\boldsymbol{v} - \boldsymbol{w}))).Grad(n\rho_f) + n\rho_f Div(\boldsymbol{v} - \boldsymbol{w}) \qquad (12)$$

$$Grad(n\rho_f) = n\frac{\partial\rho_f}{\partial p}Grad(p) + \rho_f Grad(n) = \rho_f(nC_f Grad(p) + Grad(n)) \qquad (13)$$

Substituting into Eq. 6 and combining with Eq. 8, the mass balance equation becomes:

$$S_p\frac{dp}{dt} + \alpha Div(\boldsymbol{w}) + (\boldsymbol{v} - \boldsymbol{w}))).(nC_f Grad(p) + Grad(n)) + nDiv(\boldsymbol{v} - \boldsymbol{w}))) = 0 \qquad (14)$$

Note that the change in porosity is based on elastic theory. For elastoplastic deformation, the governing equation is given in Eq. 25 in the next section.

2.2. Equation of Motion for the Solid-Fluid System

Assuming stresses in the fluid and solid are related by: $\boldsymbol{\sigma}^f \boldsymbol{n} - p\boldsymbol{n} = \boldsymbol{\sigma}^s \boldsymbol{n}$, where $\boldsymbol{n}$ is the normal unit vector, we obtain (de la Cruz and Spanos, 1989):

$$(1-n)\rho_s \frac{\partial \boldsymbol{w}}{\partial t} + n\rho_f \frac{\partial \boldsymbol{v}}{\partial t} = Div(\boldsymbol{\sigma}) + \rho g - K_s Grad(n) \qquad (15)$$

Stress in the fluid can be defined in terms of fluid velocities as:

$$Grad(\boldsymbol{\sigma}^f) = (\mu + \lambda_f)Grad(Div(\boldsymbol{v})) + \mu(Grad^2(\boldsymbol{v})) \qquad (16)$$

where superscripts s and f denote the solid and fluid phases, and $\lambda_f = -2/3\mu$ since shear stresses for fluid are assumed to be zero. Stress is then replaced by effective stress through: $\boldsymbol{\sigma}' = \boldsymbol{\sigma} - \alpha p \boldsymbol{I}$, where $\boldsymbol{I}$ is the identity matrix.

2.3. Equation of Motion for Fluid

The equation of motion for fluid is presented in differential form as (de la Cruz and Spanos, 1989):

$$n\rho_f \frac{\partial v}{\partial t} = -nGrad(p) - \frac{(n^2\mu)}{k}(\boldsymbol{v} - \boldsymbol{w}) + n\mu Div(Grad(\boldsymbol{v})) +$$
$$n[(\mu + \lambda)_f]Grad(Div(\boldsymbol{v})) + \rho_f g + \rho_{12}\frac{\partial(\boldsymbol{v} - \boldsymbol{w})}{\partial t} \qquad (17)$$

Replacing λ_f, one obtains:

$$n\rho_f \frac{\partial v}{\partial t} = -nGrad(p) - \frac{(n^2\mu)}{k}(\boldsymbol{v} - \boldsymbol{w}) + n\mu\big(Div(Grad(\boldsymbol{v})) +$$
$$\frac{1}{3}Grad(Div(\boldsymbol{v}))\big) + \rho_{12}\frac{\partial(\boldsymbol{v} - \boldsymbol{w})}{\partial t} + \rho_f g \qquad (18)$$

The added mass,ρ_{12} , comes from the tortuous path that the fluid follows to pass through the porous medium. The narrowing-widening nature of porous media makes the fluid more accelerated. In other words, it is equivalent to an increase in the fluid mass. This added mass depends on the tortuosity or connectivity of pores.

As Eq. 18 shows, the fluid momentum balance equation reduces to Darcy's law under negligible compressibility and no dynamic effect (Verruijt, 2010). A convection term, $(Div(\boldsymbol{v}))\boldsymbol{v}$, may appear in some formulations, but it is avoided here. Beck (1972) stated that this term is inappropriate since it

increases the order of the partial differential equation. It is also inconsistent with the slip boundary condition. In addition, this term is not an appropriate way to account for nonlinear drag, arising from inertial effects, since this term is zero for steady incompressible 1D flow regardless of the fluid velocity. The convection term can only be important for high-speed compressible fluid flow in highly porous medium. In general, this term will be small and can be ignored since solid structure may prohibit some motion and cause a change in momentum (Nield and Bejan, 2006).

2.4. Constitutive Law

Hook's law is used for elastic description of solid deformation.

$$\dot{\boldsymbol{\sigma}}' = (K_s - \frac{2}{3}G)\dot{\epsilon}\boldsymbol{I} + 2G\dot{\boldsymbol{\epsilon}} \tag{19}$$

where $\dot{\boldsymbol{\sigma}}'$ is the rate of change of effective stress, $\dot{\boldsymbol{\epsilon}}$ is the rate of change of strain, K_s is bulk modulus, G is shear modulus and $\boldsymbol{I}$ is the identity matrix defined before. Compressive stresses are assumed to be positive.

2.5. Mass Balance Equation for Elastoplastic Medium

For elastoplastic deformation of rock, one may expect that nearly all porosity change will be originated from bulk volumetric deformation. The assumption here is that the fluid volume change is negligible compared to that of the solid. The porosity of the rock can be calculated from:

$$n = 1 - \frac{(1 - n_0)}{(1 + \epsilon_v)} \tag{20}$$

where n_0 is the initial porosity and ϵ_v is the volumetric strain. Taking differentiation:

$$dn = \frac{(1 - n_0)}{(1 + \epsilon_v)^2}d\epsilon_v \tag{21}$$

Therefore the rate of porosity change with respect to time is:

$$\frac{dn}{dt} = \frac{(1 - n_0)}{(1 + \epsilon_v)^2}Div(\boldsymbol{w}) \tag{22}$$

where $d\dot{\epsilon}_v = Div(\boldsymbol{w})$. Mass balance equation was derived by combining Eq. 6 and Eq. 8:

$$n\rho_f C_f \frac{dp}{dt} + \rho_f \frac{dn}{dt} + n\rho_f Div(\boldsymbol{w}) + Div(n\rho_f(\boldsymbol{v} - \boldsymbol{w})) = 0 \qquad (23)$$

Substituting Eqs. 12, 13 and 22 into Eq. 23 yields:

$$\rho_f(nC_f)\frac{dp}{dt} + \rho_f \frac{(1-n_0)}{(1+\epsilon_v)^2}Div(\boldsymbol{w}) + n\rho_f Div(\boldsymbol{w}) + n\rho_f Div(\boldsymbol{v} - \boldsymbol{w}) + \qquad (24)$$
$$(\boldsymbol{v} - \boldsymbol{w}).\rho_f(nC_f Grad(p) + Grad(n)) = 0$$

Dividing by ρ_f and simplifying the equation, one obtains Eq. 25 for the fluid mass balance.

$$(nC_f)\frac{dp}{dt} + \frac{(1-n_0)}{(1+\epsilon_v)^2}Div(\boldsymbol{w}) + nDiv(\boldsymbol{v}) + (\boldsymbol{v}-\boldsymbol{w}).(nC_f Grad(p) + Grad(n)) = 0.$$
$$(25)$$

2.6. Comparison with Biot's Theory

Biot's theory neglects some physics that govern the transport phenomenon in saturated porous media. One important assumption in Biot's theory is that porosity change is ignored. This porosity change leads to a porosity diffusion wave which can play a significant role in multi-phase saturated porous medium by enhancing the transport of the non-wetting phase (Spanos et al., 1999). The other difference is the fluid compressibility terms in fluid momentum balance, $n\mu\big(Div(Grad(\boldsymbol{v})) + \frac{1}{3}Grad(Div(\boldsymbol{v}))\big)$. The effect of these differences on the results is demonstrated later in Figure 3 to Figure 5.

2.7. Artificial Viscosity Damping

In fluid dynamics, artificial viscosity is very common to damp the unrealistic oscillations resulting in a smooth response for modeling shock waves. Artificial viscosity makes it possible for the wave to be modeled by considering it as a viscous dissipation over a thin space, instead of a jump with infinitesimally small thickness. In reality, the thickness of the waves is at the molecular scales.

Artificial viscosity damping has been evolved over the years. The first representation was a scalar form in terms of the velocity rate. It includes the Von Neumann term, q_1, and the Landshhoff term, q_2 which are given by (Wilkins, 1980):

$$q_1 = -sign(\dot{\epsilon}_v)c_0^2\rho L^2 {\dot{\epsilon}_v}^2$$
$$q_2 = -sign(\dot{\epsilon}_v)c_L \rho La\dot{\epsilon}_v \qquad (26)$$

where L is element size, $\dot{\epsilon}_v$ is the rate of volumetric strain, c_0 and c_L are constant values equal to 2 and 1 respectively, a is the speed of sound which is equal to $\sqrt{((K_s + 4/3G)/\rho)}$ (Wilkins. 1980), q_1 is the Von Neumann term which damps the oscillations behind the front and spreads the wave over the mesh, q_2 is the Landshhoff term which diffuses the shock front over an increased number of zones as the shock wave progresses (FLAC user manual, 2008). The minus sign of volumetric strain ensures that damping always occur in the opposite direction of the strain.

This damping is a scalar value which is used in the calculation of stress gradients. For a 2D case, the tensor form of artificial viscosity is adopted here based on the original scalar form:

$$
\begin{aligned}
q_{r1} &= -sign(\dot{\epsilon}_{rr})c_0^2\rho\delta r^2\dot{\epsilon}_{rr}^2 \\
q_{r2} &= -sign(\dot{\epsilon}_{rr})c_L\rho\delta ra\dot{\epsilon}_{rr}
\end{aligned}
\tag{27}
$$

$$
\begin{aligned}
q_{z1} &= -sign(\dot{\epsilon}_{zz})c_0^2\rho\delta z^2\dot{\epsilon}_{zz}^2 \\
q_{z2} &= -sign(\dot{\epsilon}_{zz})c_L\rho\delta za\dot{\epsilon}_{zz}
\end{aligned}
\tag{28}
$$

$$
\begin{aligned}
q_{\theta1} &= -sign(\dot{\epsilon}_{\theta\theta})c_0^2\rho r^2\dot{\epsilon}_{\theta\theta}^2 \\
q_{\theta2} &= -sign(\dot{\epsilon}_{\theta\theta})c_L\rho ra\dot{\epsilon}_{\theta\theta}
\end{aligned}
\tag{29}
$$

$$
\begin{aligned}
q_{rz1} &= -sign(\dot{\epsilon}_{rz})c_0^2\rho(w_{z_{i+1,j}} - w_{z_{i-1,j}} + w_{r_{i,j+1}} - w_{r_{i,j-1}})^2/4 \\
q_{rz2} &= -sign(\dot{\epsilon}_{rz})c_L\rho(w_{z_{i+1,j}} - w_{z_{i-1,j}} + w_{r_{i,j+1}} - w_{r_{i,j-1}})/2
\end{aligned}
\tag{30}
$$

Comparing the smoothness of the results for the discussed artificial viscosities, this tensor form is more effective than the scalar form in damping numerical oscillations of 2D problems.

2.8. Discretization and Solution Method

Appendix A extends the equations to cylindrical coordinates for axisymmetric condition. The finite difference method was used to solve the equations sequentially using the velocity-stress scheme (Virieux, 1986). The solution method is described in details in Appendix B.

3. Validation against Experimental Data

van der Grinten et al. (1985) and van der Grinten et al. (1987) conducted a shock tube study by applying a single step-like pore pressure wave to a cylindrical sand sample and measuring the pore pressure at different locations

from the top of the sample. There was a layer of water on top of the sample to ensure full saturation and above that there was a plastic sheet separating a high-pressure section from a low-pressure part in the tube. To produce the shock wave, the sheet was burned and a plane wave hit the water surface above the sample. This induced a step-like pore pressure increase. The schematic of the experiment is shown in Figure 1.

There was a thin water layer (1 mm) separating the sample from the shock tube preventing shear interaction between the wall and the sample. To measure pore pressure, the pressure gauges have been placed in the gap resulting in erroneous measurements caused by wave propagation in the water column. For instance, Wisse (1999) performed two similar tests one with small (0.25 mm) and the other with large (3.5 mm) gaps and stated that over the entire frequency ranges the gap pressure and the porous sample pressure have the same order of magnitude. However the results of the small-gap measurements were closer to theoretical predictions. North (2002) performed a 2D modelling of both water and porous media using Biot's theory and concluded good agreement between the results of the theoretical model and the measurements of the shock tube for tests with small gap. However, for large gap sizes between the sample and shock tube, the wave in the water has an impact on the amplitude of the measurements. No explanation of the gauge placement was provided in van der Grinten et al. (1985). However, in a later work, they measured both pore pressures in the gap and in the sand sample using identical experimental set-ups (van der Grinten et al., 1987). This newer experiment also included strain measurements. Hence, we used the later work which used the same type of soil as in their earlier work to validate the simulator developed here.

The soil properties are summarized in Table 1. The compressibility of the sand grain is not reported in the experiment. A value of 2.35×10^{-11} 1/Pa, which is the average of grain compressibility values reported for Ottawa sand and quartz from Gulf of Mexico, is used in the modeling (Richardson et al., 2002). The sample was saturated with water whose properties were not measured. As such, typical water properties are assigned in the model (i.e. density=1000 kg/m^3; viscosity=1 cp; bulk modulus=2 GPa).

3.1. Comparison of Simulation and Experimental Results

Figure 2 shows the schematics of the model under 2D axisymmetric condition. The sample size is 75 mm in diameter and 1.895 m in length. Very fine mesh is required for the convergence of the solutions and to capture the wave
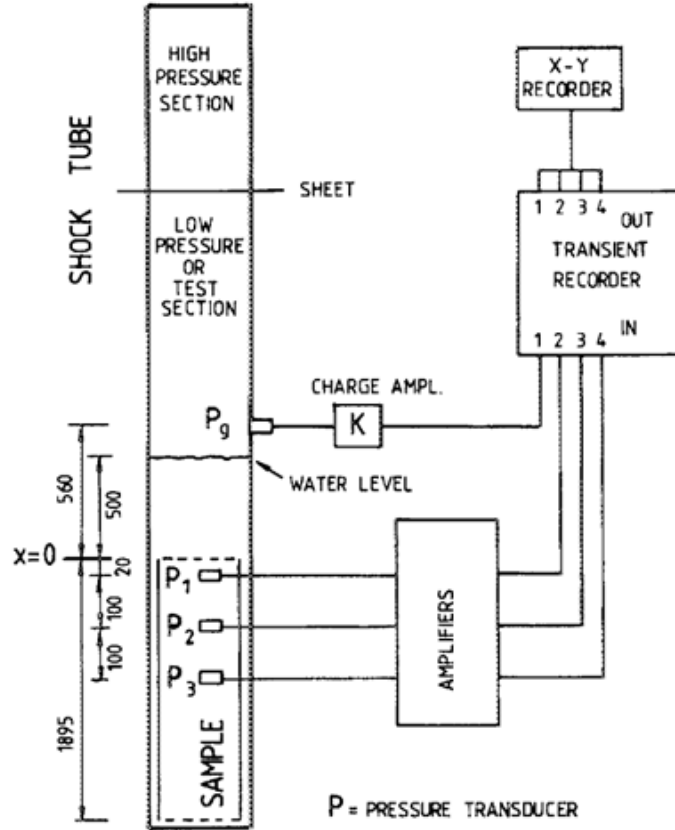
Figure 1: Shock tube experiment (van der Grinten et al., 1985)

Table 1: Properties of the porous sand (van der Grinten et al., 1985)

Property	Value
Sand Intrinsic density (kg/m^3)	2650
Bulk Modulus (GPa)	8.16
Shear Modulus (GPa)	1.3
Permeability (m^2)	5.62×10^{-11}
Porosity	0.3
Added mass parameter	2.7

propagation through the sample. For this work the radius and the length were divided into 10 and 400 equal elements, respectively, following a mesh

sensitivity analysis. The time step was selected so that the waves travel the length of one element during one time step. The bottom of the model was assumed to be fixed in the vertical direction and the shock wave was applied from the top. This shock wave was represented by a combination of pore pressure and normal stress waves, i.e. zero effective stress normal to the top surface. The right boundary was allowed to move freely in the model in r direction while in the experiment water would prevent some (but not all) of the displacements.
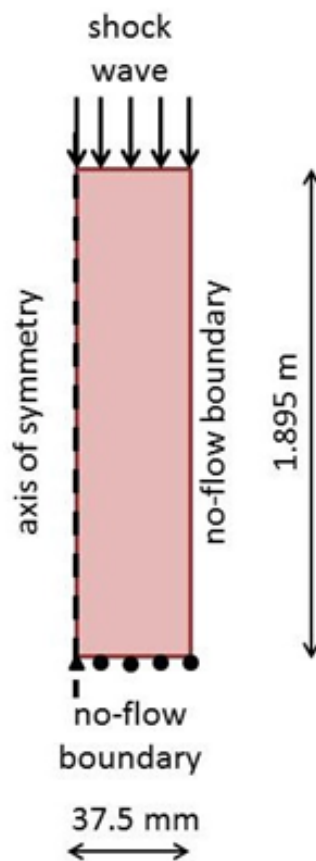
Figure 2: Schematic of the model geometry

Figure 3 shows two jumps in the pore pressure response. It is hypothesized that (1) the first jump is the result of an undrained wave where both phases move together while the sample is contracted under the shock load; and (2)

the second jump is due to deceleration of solid velocity while fluid phase is accelerating (See Figure 6).

Figure 3 through 8 show the results of the numerical model, which indicate a reasonable agreement between the measured and calculated pore pressures at 120 and 220 mm from the top. Note that we used the tortuosity (or added mass) as a calibration parameter to obtain a closer match for the pore pressures because among the measured properties tortuosity has the highest uncertainty. This parameter is characterized by electrical conductivity measurements as suggested by Brown (1980). However, this measurement method is valid as long as the pore structure can be assumed incompressible, and would also be erroneous when applied to deformable porous media. The effect of tortuosity on the simulation results is viewed in **??**
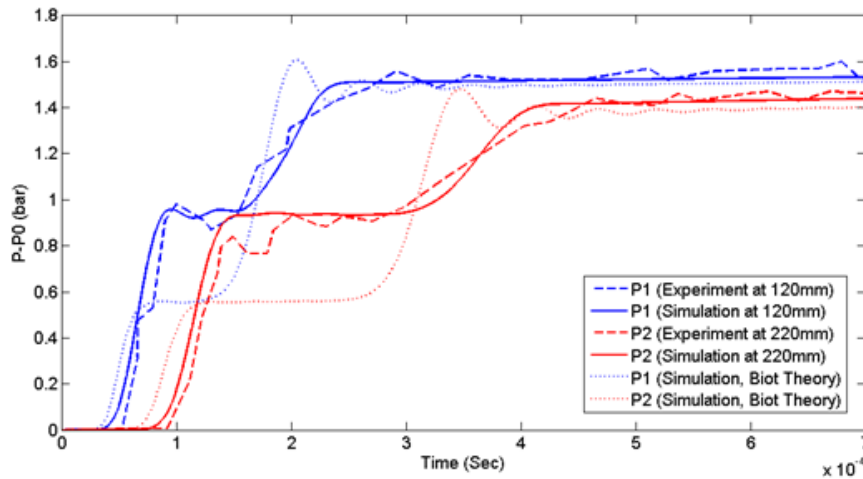
Figure 3: Comparison of measured and calculated pore pressure response for a shock wave

Figure 3 to Figure 5 show noticeable difference between the predictions of Biot's theory and the formulation used in this work during the transient period. Biot's theory prediction for the amplitude of the undrained wave is nearly half of the real value. Note that changing the value of tortuosity does not improve the results obtained by Biot's theory since tortuosity has no effect on the speed of the first wave which is overestimated by Biot's theory. Van der Grinten et al. (1985) and van der Grinten et al. (1987) attributed the difference to the radial motion of the sample and, therefore, modified the constrained modulus,$K_s + 4/3G$, to an effective constrained

13

modulus (4.5 GPa instead of 9.9 GPa) in their analytical model. We will see that the radial motion of the sample in this experiment is negligibly small. Also the rise of the second wave as predicted by Biot's theory is more abrupt than the predictions of Spanos and De la Cruz's theory and the experimental measurements.

The strain gauges inserted on the wall of the sample are pressure-dependent because they are glued to the porous sample with epoxy resin whose bulk modulus is smaller than that of the sand. Therefore, the glue would be compressed with increasing pressures. This pressure dependency was calculated from separate experiments. Values of 3.5 and 5.0 microstrain/bar are reported for the pressure sensitivity of these gauges (van der Grinten et al., 1987). Both the measured values and the corrected ones are shown in Figure 4 and Figure 5 assuming compressive strains to be positive. There is a difference in the transient regime but the trend is predicted correctly. This difference is more significant using Biot's theory.

Figure 6 and 7 show the axial velocity and acceleration of both phases at 220 mm from the top of the sample, respectively. The interesting point is that solid and fluid phases move together in the beginning resulting in undrained wave propagation due to undrained conditions (Verruijt, 2010). For the second wave, the phases move with opposite accelerations with larger differences in velocities. Therefore, the friction between the two phases leads to the damping of wave amplitude far from the source.
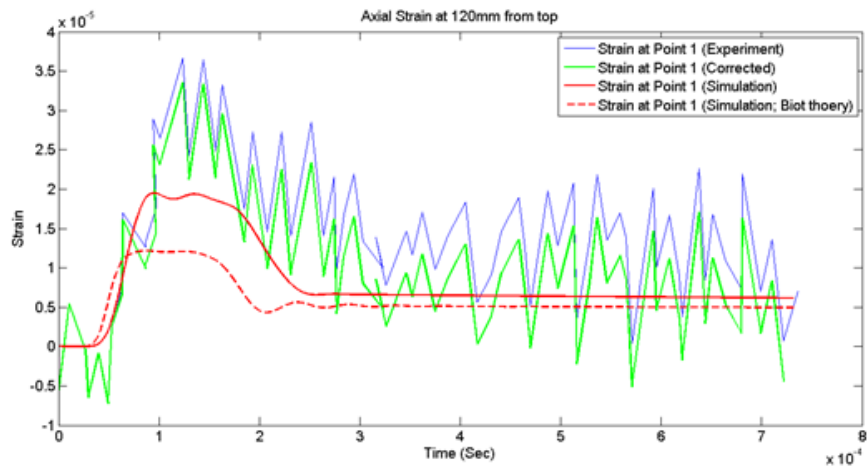
Figure 4: Comparison of axial strain response at 120mm from the top of sample

14
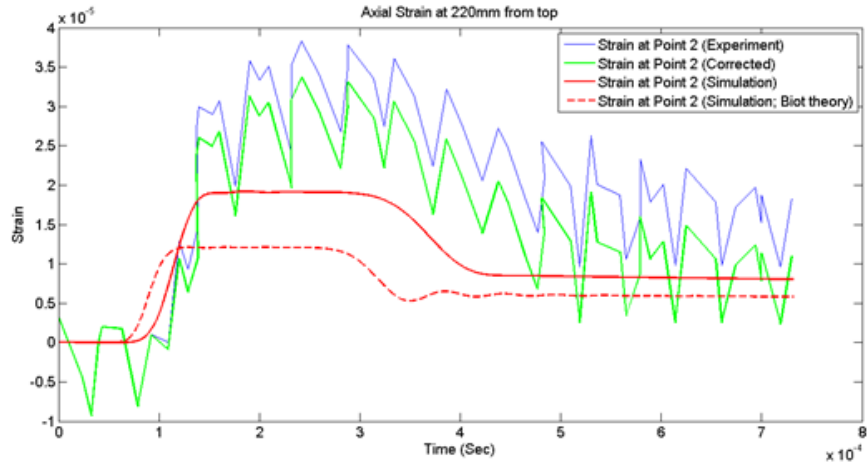
Figure 5: Comparison of axial strain response at 220mm from the top of sample
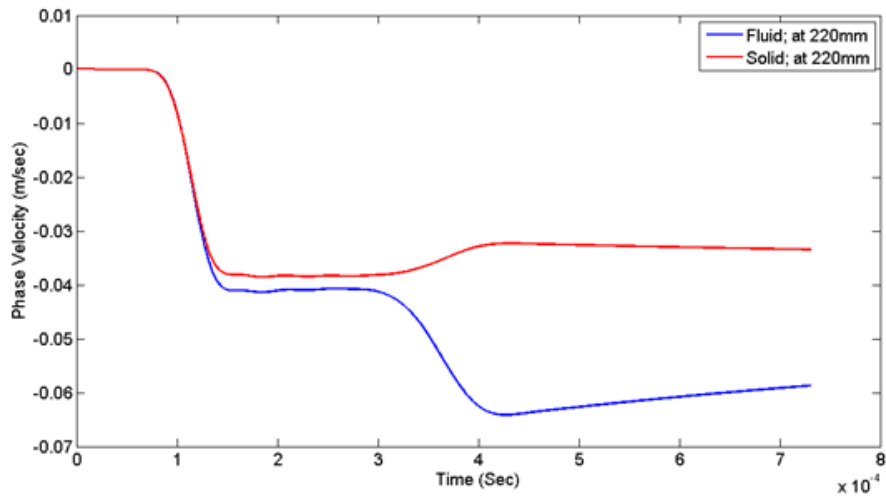
Figure 6: Simulated axial velocity response at 220mm from the top of sample

Simulation results indicate near zero values for radial acceleration and velocity. Therefore, it appears that the radial motion of the sample does not play a significant role in this experiment which is contrary to the justification for wave speeds done by van der Grinten et al. (1985) and van der Grinten et al. (1987).

It would be beneficial to look at the porosity changes during wave prop-

15
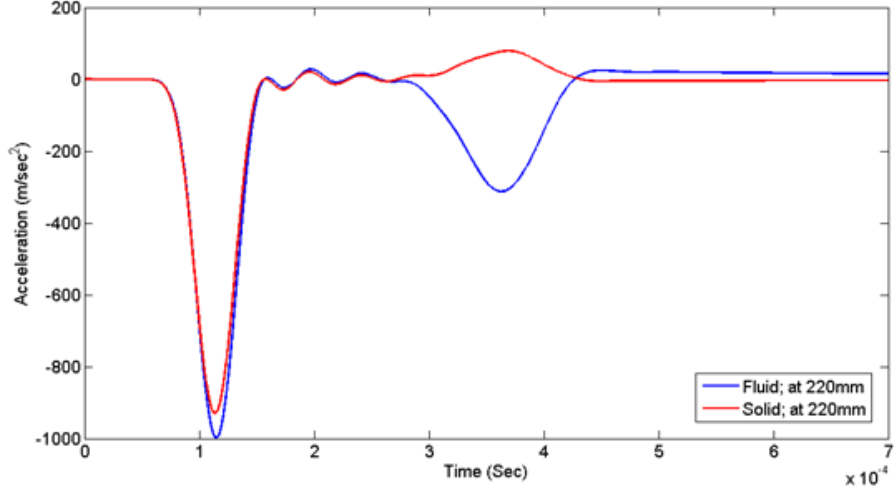
Figure 7: Simulated axial acceleration response at 220mm from the top of sample

agation. Figure 8 shows the time variation of normalized porosity as defined by $n_D = (n - n_0)/n_0$. The first drop in porosity is the result of the sample contraction due to the shock wave. The subsequent increase in porosity is the result of the second wave when the solid moves more slowly than the fluid resulting in some expansion but not enough to cancel out all the initial contraction.

Figure 9 shows the effect of tortuosity on the numerical results. It affects the amplitude of the first wave and the speed of the second wave. Tortuosity or the narrowing-widening nature of porous media makes the fluid more accelerated. This acceleration can generate a wave with different amplitude.

3.2. Wave Reflection in the Shock Tube

Verruijt (2010) presented an analytical solution to Biot's 1D dynamic formulation for a shock pore pressure wave and estimated the velocity of both waves. The solutions predict nearly the same velocities for the fluid and solid phases ($\boldsymbol{w} \sim \boldsymbol{v}$) under undrained conditions and elastic solid. It also predicts the wave propagation at the velocity of c_1 given by:

$$c_1 = \sqrt{((k_u + \frac{4}{3}G)/\rho)} \tag{31}$$

where k_u is the undrained bulk modulus of the soil.

16
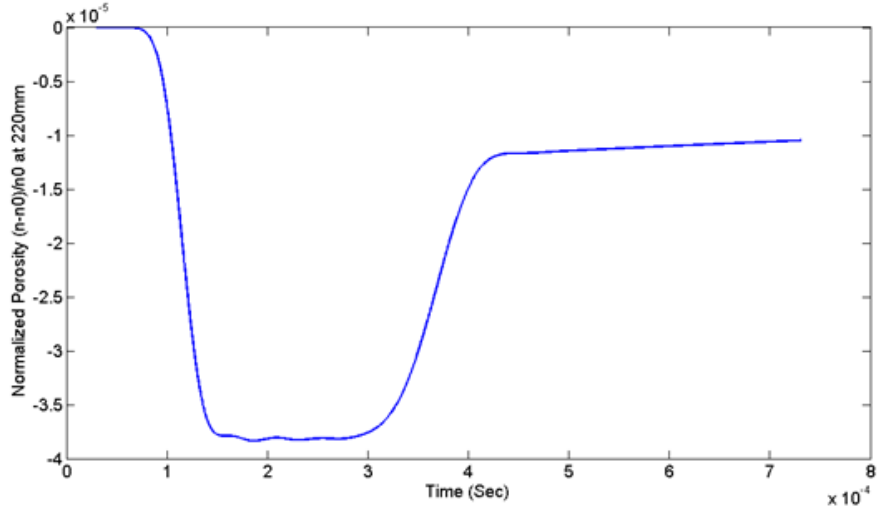
Figure 8: Change of porosity due to a shock wave
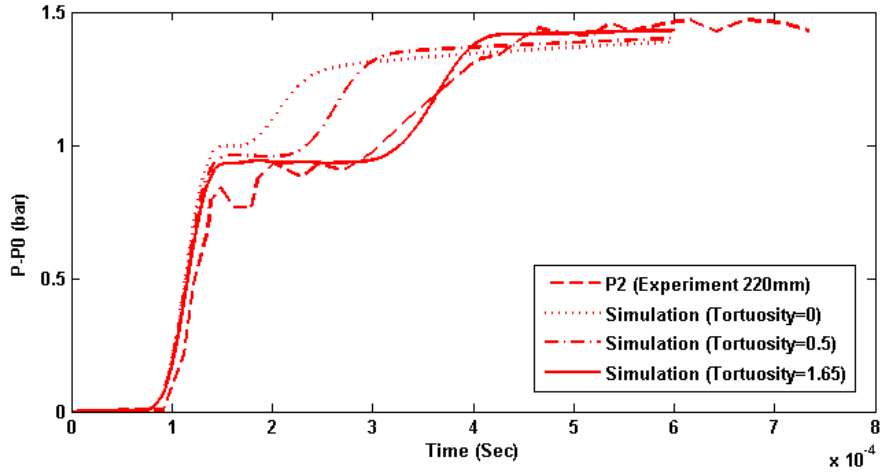
Figure 9: Effect of tortuosity

The second wave speed for very high frequencies is estimated by:

$$c_2 = \sqrt{(n/[(1+\tau)\rho_f S_p])} \tag{32}$$

which is the same as the propagation wave velocity in fluids. τ in this equation represents the tortuosity.

17

Equations 31 and 32 result in the velocities of 2508 m/sec and 732 m/sec for the solid and fluid waves, respectively. Hence, the time for the solid and fluid waves to travel to the bottom end of the sample and return to point 2 (220 mm from top) is estimated to be 0.0014 sec and 0.0049 sec respectively. Using the simulation results, the wave velocities are calculated as 1980 m/sec for solid and 649.9 m/sec for fluid waves. Therefore, the time needed for the reflected wave in the solid and fluid to reach Point 2 is estimated at 0.00184 and 0.0058 sec respectively. This assessment is in agreement with Figures 10 and 11, which show the wave reflection in terms of pore pressure and porosity. The vertical lines represent the expected reflection times calculated from the wave velocities. It seems there is a slowing factor as time increases. The figure shows only the first wave reflection and there are no pressure changes at the expected reflection times of the second wave. This wave is usually damped far from the source (Verruijt, 2010). In addition, the type of the boundary plays an important role into whether a wave is reflected or completely absorbed. The velocity of the first wave depends only on the moduli and the density of the medium. Density especially that of the fluid, increases with higher pressure resulting in a slightly slower wave. This is why based on the first wave speed the reflections should occur slightly earlier. Figure 11 shows
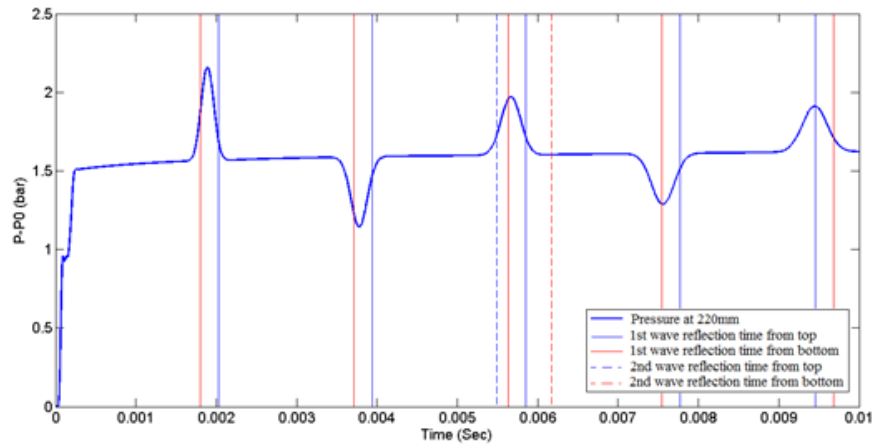
Figure 10: Pore pressure response due to the reflection of wave at 220mm (P2) from the top of the sample

that the reflection of wave can also be observed by examining the porosity changes. The first drop in porosity is the result of the first undrained wave
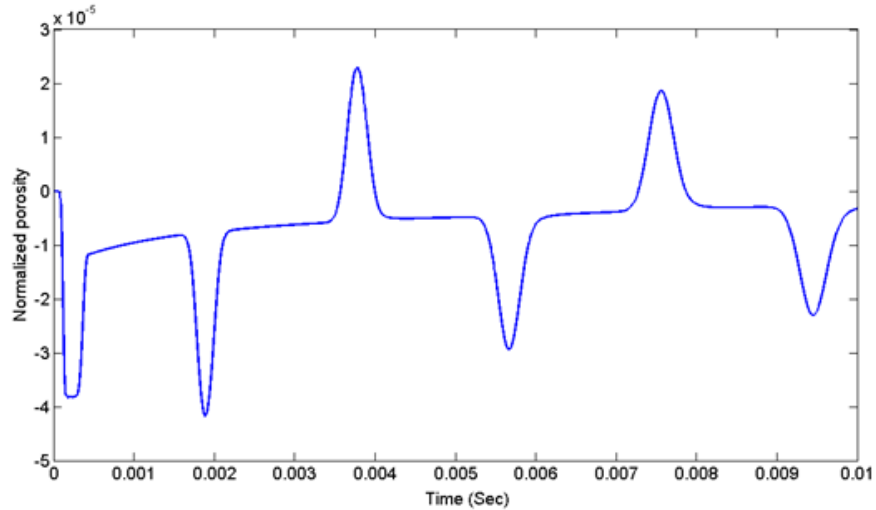
Figure 11: Porosity response due to the reflection of wave at 220mm from the top of the sample

followed by an increase in porosity by the second wave to an approximately steady value. The later changes are due to the reflection of the first wave.

Figure 12 demonstrates the axial displacements through time. Initially, downward displacements are generated as the waves compress the soil sample. After a while, when the wave hits the boundary and is reflected, part of the compression is relieved.

4. Waterhammer Waves

Waterhammer (WH) is a general term describing pressure wave generation and propagation through liquids in pipes and pipe networks (Jardine et al., 1993). The classic analysis of waterhammer shows that a pressure pulse is generated when the flow is suddenly stopped, e.g. a valve is closed. Pressure increases upstream of the valve and reduces on the downstream side of the valve. The liquid then comes to complete halt downstream to the valve resulting in the flow from the reservoir into the pipe and acceleration of the fluid towards the valve, resulting in a high-pressure pulse. The pulsation travels back and forth in the pipe until it is fully attenuated by the wall friction, and pipe deformation among others (McStravick et al., 1992).

The magnitude of initial waterhammer amplitude can be estimated using

19
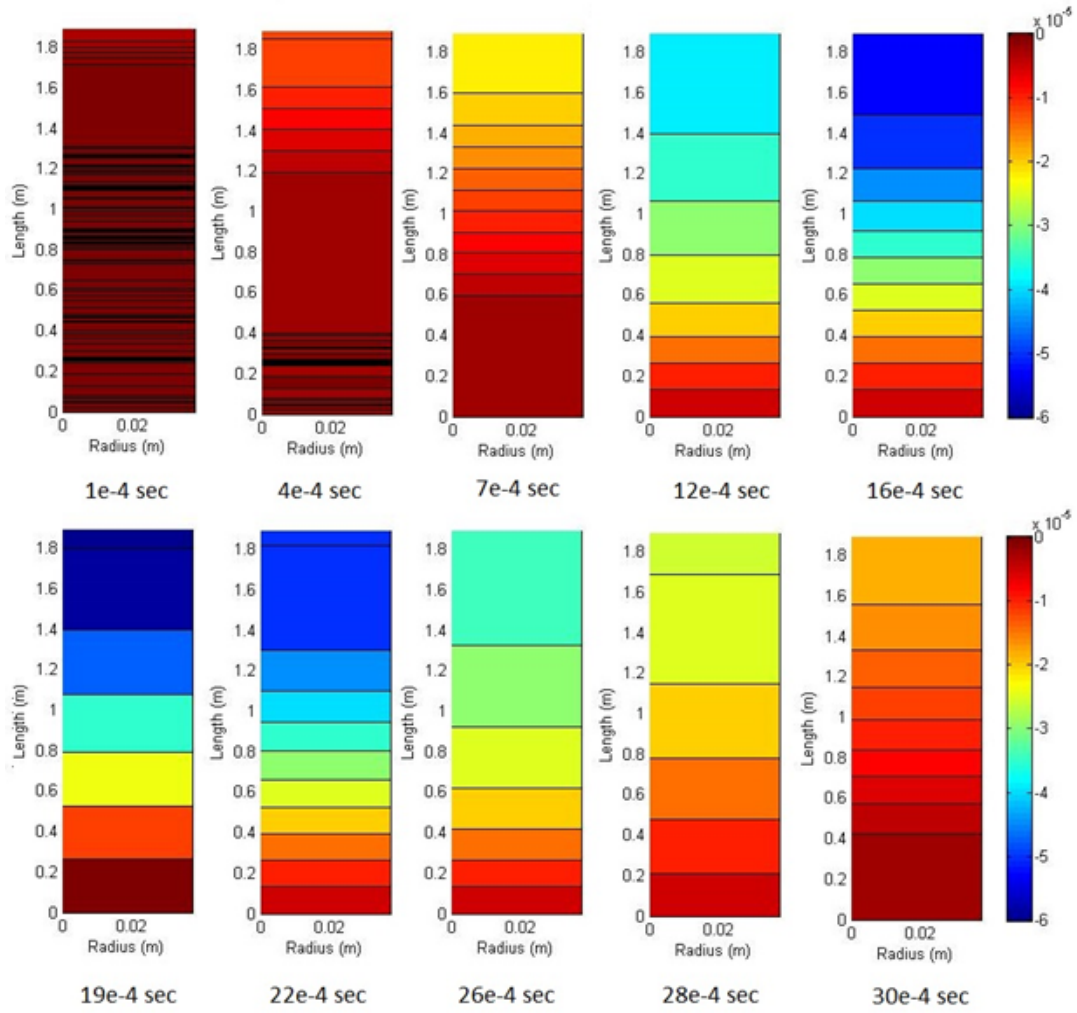
Figure 12: Contours of axial displacement

(Streeter et al., 1998):

$$\Delta p_{max} = \rho c \Delta v \qquad (33)$$

where c is the speed with which the pressure-pulse wave is transmitted along a pipe and is calculated using (Streeter et al., 1998):

$$c^2 = \frac{(\frac{K_f}{\rho})}{(1 + (\frac{K_f}{E})(\frac{D}{l}))} \qquad (34)$$

20

where K_f is the bulk modulus of elasticity of the fluid, E is the elastic modulus of the pipe, D is the inner diameter of the pipe and l is the thickness of the pipe. The basic equations in formulating waterhammer analysis are Newtons second law and the continuity equation.

Waterhammer waves can be generated in an oil well due to sudden shut-in caused by pump malfunctions, sudden shut-in in emergency situations to prevent blow-out, velocity changes due to step-rate-testing (SRT), sudden shut-in during a pressure build-up test and sudden changes in flow rate during injection/production cycles. They may also be generated during drilling operations by a kick, tripping out, pulling the string, casing, or even screens (Hayatdavoudi, 2005). Waterhammer effects resulting from the shutting in of water injection wells are often ignored in petroleum production operations but they can result in considerable impact on the performance and longevity of the injection well (Wang et al., 2008). Waterhammer pulses hit the reservoir formation like seismic waves during shut-in and may lead to liquefaction of sand (Santarelli et al., 2000). As a result, sudden shut-in of the well should be avoided unless in an emergency. Wang et al. (2008) reported the measurements of waterhammer pulses in an Alaskan oil field by downhole memory pressure gauges. They examined the repeatability of the wave characteristics by repeating the test. They measured waterhammer waves with frequencies as high as 17 Hz. Waterhammer is a short transient event and its modeling requires the use of a dynamic approach.

4.1. Waterhammer Pressure Propagation in Porous Media

The results of the simulation of the propagation of a shock wave in a hypothetical reservoir are presented in this section. Since the emphasis of this work is on dynamic fluid flow and wave propagation through porous media, the rock deformation is assumed to be elastic obeying Hook's law. Hence, there is no attempt to incorporate failure or any possible liquefaction of the rock. The reservoir properties are: zero tortuosity, 500 mDarcy permeability, bulk modulus of 218 MPa and shear modulus of 131 MPa. All the other properties are the same as those of the experiment cited before. In-situ reservoir pressure and vertical and horizontal stresses were selected to be 112, 120 and 115.6 MPa, respectively. The injection into the reservoir was applied from an openhole with the diameter of 10 cm at the pressure of 115.6 MPa. The right boundary was fixed against displacement in the normal direction and the pore pressure was also fixed in the same boundary. The initial condition was considered to be steady-state injection and axial symmetry

21
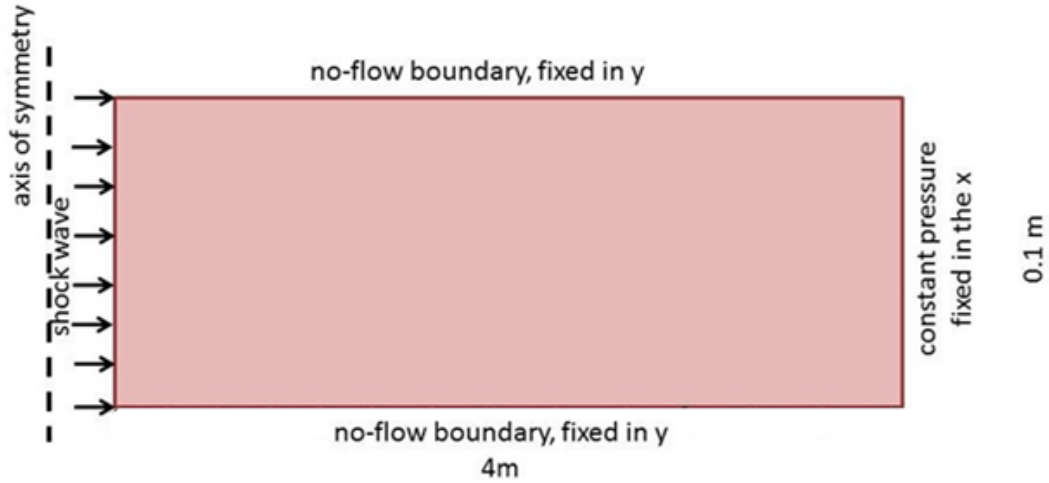
Figure 13: Schematic of the reservoir model

was assumed. A drop wave with amplitude of 3.6 MPa was applied on the wellface. The total stress at the wellbore was also dropped simultaneous to the pressure drop so that the effective stress stayed at $(1 - \alpha)p$, where α is the Biot's constant.

Figure 14 shows the pore pressure variation with time at three different locations. The two distinct pore pressure waves are characteristics of porous media which are expected here. However, the second wave is damped in most cases and its appearance depends on the properties of the medium. The predicted velocities show that the two phases are moving together, emphasizing that only the undrained wave occurs under these conditions.

For a cylindrical wave there will be a geometric damping as the area exposed to the wave increases with radius. Hence the amplitude of the wave decreases with radius. In addition, for low permeabilities, the radius of drainage for Darcy flow cannot reach the wave front. Therefore, there will be gradual increase of the pore pressure behind the wave front. If we use the properties of the shock tube example, there will be two-wave response for the radial propagation of wave.

From the results one can observe that, in this case, only near-well areas are affected by dynamics. Figure 14 shows that only one fifth of the applied wave is expected one meter away from the well. However the nature of the wave is very quick and when the wellbore is exposed to subsequent multiple

22

waves, e.g., for waterhammer pressure pulsing, dynamic analysis is necessary to obtain a proper solution for the problem. The change in the effective
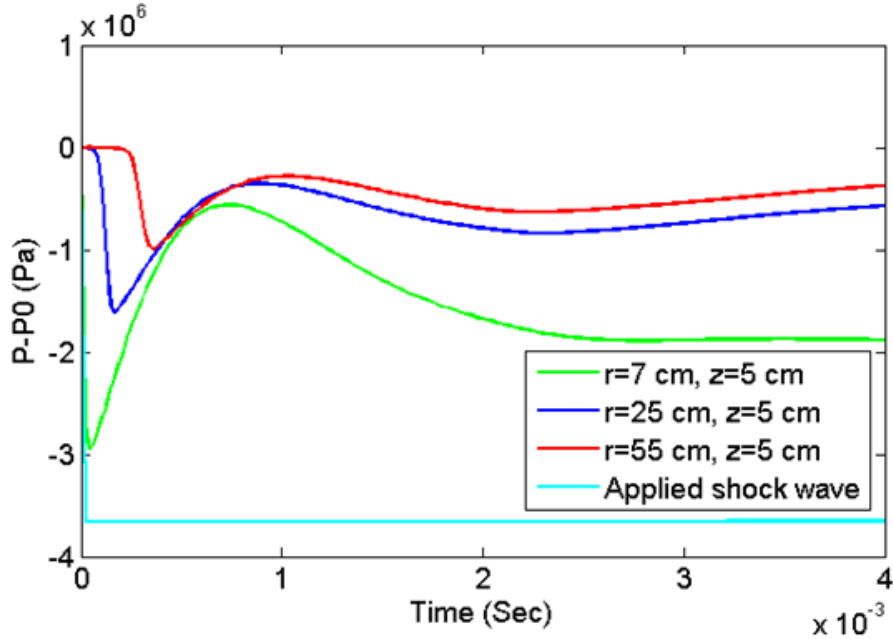
Figure 14: Pore pressure versus time at three locations

stresses and shear stress are plotted in Figure 15 through 17. Although pore pressures return to their original values when the waves are damped, effective radial stresses undergo a permanent change.

Since we are modeling a 2D problem, we should expect to observe the generation and travel of shear waves in the model. A shear wave is a wave for which the direction of particle displacement is perpendicular to the wave traveling direction. Here we have a radial wave; under axisymmetric conditions, the shear wave must induce oscillating vertical displacements, equivalent to ϵ_{rz}, Figure 18 shows the shear strain. The values of shear strain and stress are small here. This could be due to the fixed top and bottom boundaries and small reservoir thickness. More investigations are required to see if the shear stresses increase in case there is a soft cap rock on the top.

23
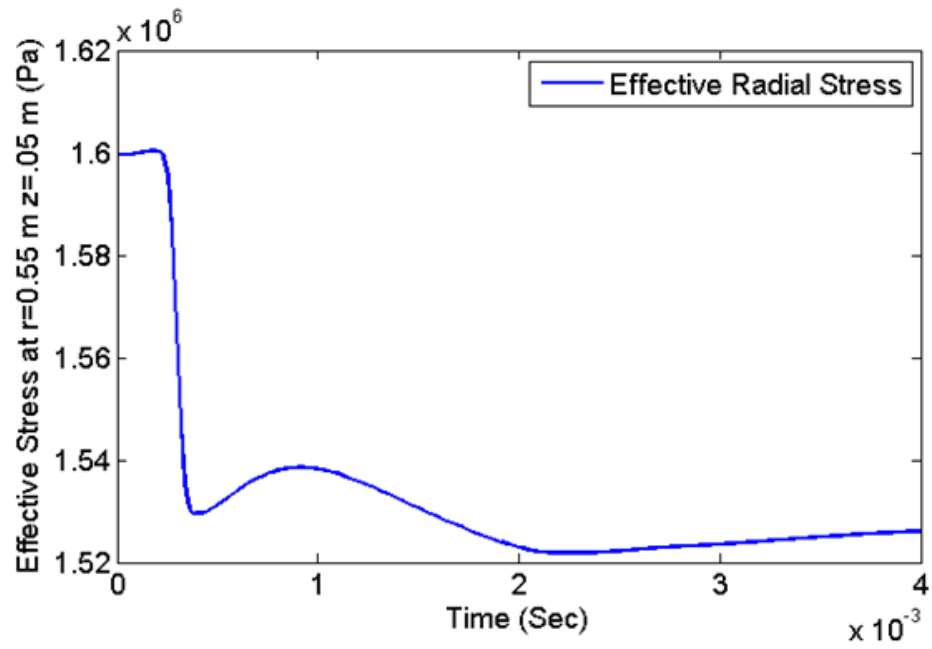
Figure 15: Effective radial stress at r=0.55 m and z=0.05 m
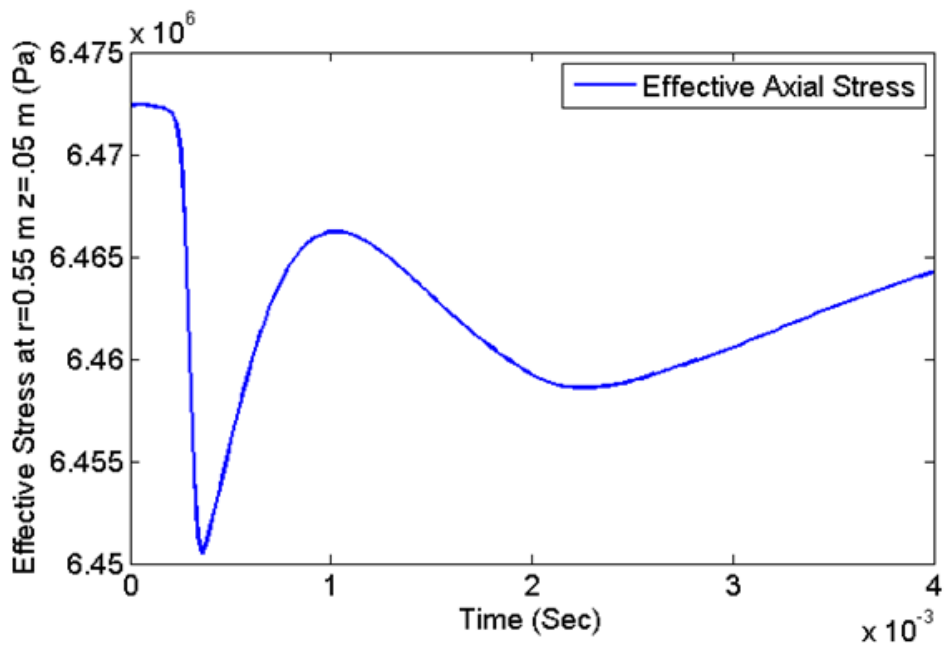
Figure 16: Effective vertical stress at r=0.55 m and z=0.05 m
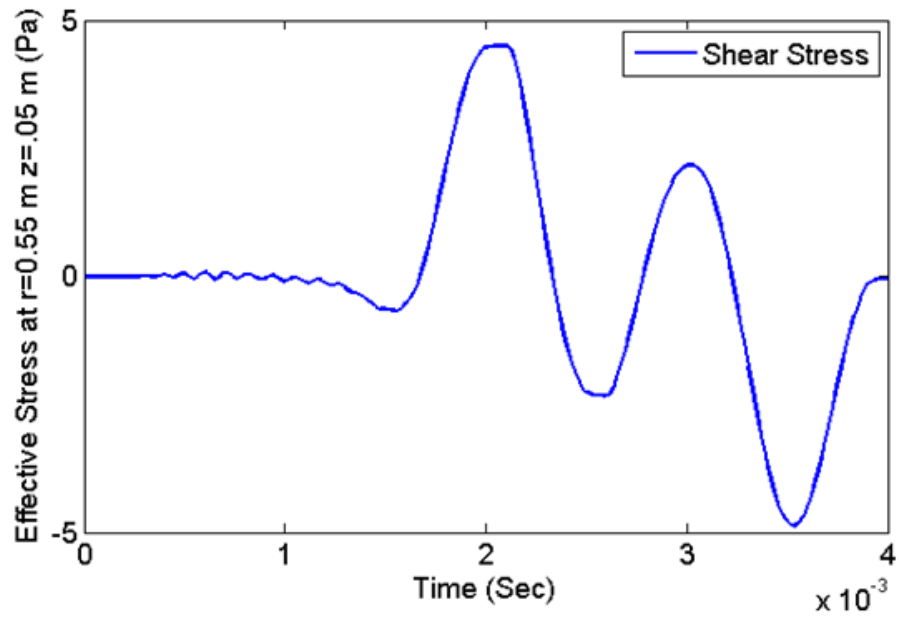
Figure 17: Shear Stress at r=0.55 m and z=0.05 m
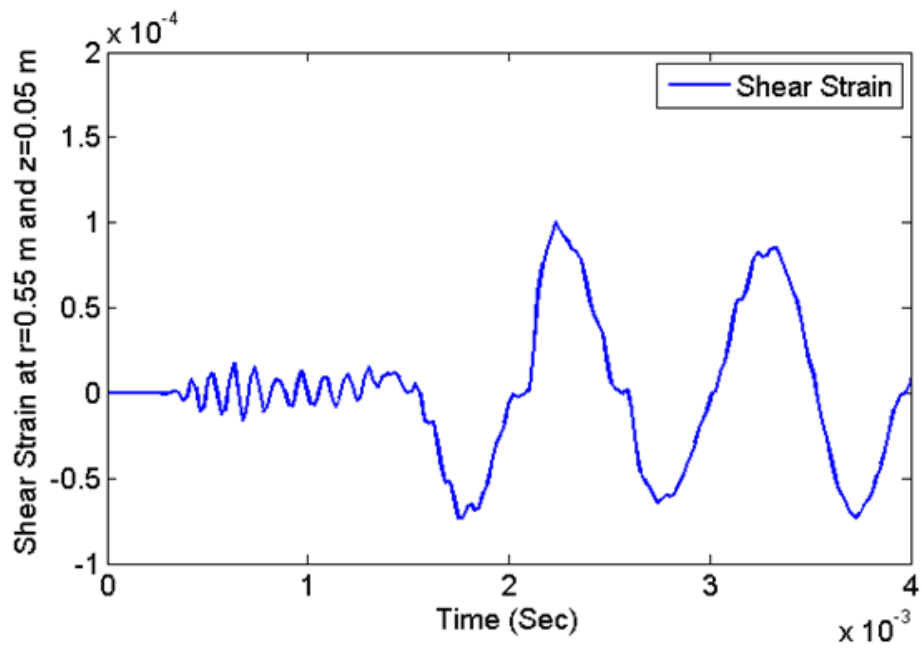
Figure 18: Shear Strain at r=0.55 and z=0.05

25

5. Conclusions

A two-dimensional mathematical formulation and numerical solution of dynamic wave propagation in saturated porous media was presented for low frequency waves with the emphasis on pore pressure waves. To predict the dynamic transient fluid flow accurately, Spanos and de la Cruz approach was adopted. The formulation was modified in displacement-stress format and the equations and the solution method are extended for elastoplastic solid behaviour. A new tensor from of artificial viscosity was proposed which is more efficient in damping numerically-induced oscillations than the original Von Neumann and Landshhoff terms.

The formulation was validated against experimental data and then compared with the formulation presented earlier by Biot. Biot's theory has shown to be inaccurate in calculating wave propagation speed in deformable porous media and the amplitudes of pore pressure responses. However, it is sufficient in predicting the trends of pore pressure.

Both theories predict two distinct waves as a result of a shock pore pressure wave: (1) undrained wave, and (2) a wave which is highly damped due to opposite motion of the solid and the fluid. The presence of this wave depends on the porous media properties.

Finally, a reservoir response to water hammer pressure wave was simulated. Only near-wellbore areas could see the dynamic effect. In rocks with low permeability (compared to soil in the shock tube experiment), Darcy's flow cannot compensate the pressure increase as quickly as the wave propagates. Consequently, the pore pressure will return to the original values after the waves pass that specific location. In 2D problems, a shear wave is also generated as a result of the shock wave.

26

Nomenclature

a	Speed of wave through solid
c	Speed of wave through pipe
C_f	Fluid compressibility
C_m	Porous medium compressibility
C_s	Grain compressibility
D	Inner diameter of the pipe
E	Young modulus of pipe
G	Shear modulus
I	Identity matrix
k	Permeability
K_s	Bulk modulus of solid
K_f	Bulk modulus of fluid
l	Thickness of pipe
n	Porosity
n_0	Initial Porosity
n_D	Dimensionless Porosity
p	Pore pressure
p_0	Initial pore pressure
p_a	Applied pore pressure
p_D	Dimensionless pore pressure
q_1	Landshhoff term in artificial viscosity damping
q_2	Von Neumann term in artificial viscosity damping
r	Radial direction
S_p	Storativity of the porous medium
t	Time
$\boldsymbol{v}_r$	Fluid velocity in r direction
$\boldsymbol{v}_z$	Fluid velocity in z direction
$\boldsymbol{w}_r$	Solid velocity in r direction
$\boldsymbol{w}_z$	Solid velocity in z direction
z	Vertical direction
α	Biot's coefficient
ϵ_v	Volumetric strain
$\dot{\boldsymbol{\epsilon}}$	Strain rate
μ	Fluid viscosity
ρ_f	Fluid density
ρ_s	Solid density
ρ_{12}	Added mass density
τ	Tortuosity
$\boldsymbol{\sigma}$	Stress tensor
$\bar{\sigma}$	Mean stress; $\bar{\sigma} = \sigma_{ii}/3$
θ	Tangential direction

References

[1] Beck, J.L. 1972. Convection in a Box of Porous Material Saturated with Fluid. Physics of Fluids (1958-1988) 15 (8): 1377-83. doi: http://dx.doi.org/10.1063/1.1694096.

[2] Biot, M.A. 1956a. Theory of Propagation of Elastic Waves in a FluidSaturated Porous Solid. I. LowFrequency Range. The Journal of the Acoustical Society of America 28 (2): 168-78. doi: http://dx.doi.org/10.1121/1.1908239.

[3] Biot, M.A. 1956b. Theory of Propagation of Elastic Waves in a FluidSaturated Porous Solid. II. Higher Frequency Range. The Journal of the Acoustical Society of America 28 (2): 179-91. doi: http://dx.doi.org/10.1121/1.1908241.

[4] Biot, M.A. 1941. General Theory of Three-Dimensional Consolidation. Journal of Applied Physics 12 (2): 155-64. doi: http://dx.doi.org/10.1063/1.1712886.

[5] Brown, R.J.S. 1980. Connection between formation factor for electrical resistivity and fluid-solid coupling factor in Biot's equations for acoustic waves in fluid-filled porous media. Geophysics 45 (8): 1269-75.

[6] Cheng, A. H. D. (1986). Effect of sediment on earthquake-induced reservoir hydrodynamic response. Journal of engineering mechanics, 112(7), 654-665.

[7] de la Cruz, V. and Spanos, T.J.T. 1989. Thermomechanical coupling during seismic wave propagation in a porous medium. Journal of Geophysical Research: Solid Earth 94 (B1): 637-42.

[8] Desai, C. S., Galagoda, H. M. (1989). Earthquake analysis with generalized plasticity model for saturated soils. Earthquake engineering and structural dynamics, 18 (6): 903-919.

[9] FLAC user manual, version 6.0 2008., 4th edition. Minneapolis, Minnesota, USA: Itasca Consulting Group Inc.

[10] Hayatdavoudi, A. 2005. Formation Sand Liquefaction: A Mechanism for Explaining Fines Migration and Well Sanding. Journal of Energy Resources Technology 127 (3): 181-90.

[11] Hill, R. 1962. Acceleration waves in solids. Journal of the Mechanics and Physics of Solids 10 (1): 1-16.

[12] Jardine, I.S., Johnson, B.A., White, B.D. and Stibbs, W. 1993. Hard or Soft Shut-in: Which Is the Best Approach? Presented at the SPE/IADC Drilling Conference, 01/01/1993.

[13] Lakes, R., Yoon, H. S., Katz, J. L. (1986). Ultrasonic wave propagation and attenuation in wet bone. Journal of biomedical engineering, 8(2), 143-148.

[14] McStravick, D.M., Rothers, D. and Blum, G. 1992. Laboratory Testing of Reflected Pressure Pulses in Small-Diameter Tubing. Presented at the Offshore Technology Conference, 01/01/1992.

[15] Nield, D.A. and Bejan, A. 2006. Convection in Porous Media: Springer. North, R.E., 2002. Numerical modeling of pore pressure on a porous rock placed in a shock tube.

[16] Plona, T.J., 1980. Observation of a second bulk compressional wave in a porous medium at ultrasonic frequencies: Applied Physics Letters, 36, 259-261.

[17] Richardson, M.D., Williams, K.L., Briggs, K.B. and Thorsos, E.I. 2002. Dynamic measurement of sediment grain compressibility at atmospheric pressure: acoustic applications. Oceanic Engineering, IEEE Journal of 27 (3): 593-601.

[18] Santarelli, F.J., Skomedal, E., Markestad, P., Berge, H.I. and Nasvig, H. 2000. Sand Production on Water Injectors: How Bad Can It Get? (06).

[19] Santarelli, F.J., Sanfilippo, F., Embry, J., White, M. and Turnbull, J.B. 2011. The Sanding Mechanisms of Water Injectors and their QUantification in Terms of Sand Production: Example of the Buuzard Field (UKCS). Presented at the SPE Annual Technical Conference and Exhibition, 01/01/2011.

[20] Sivrikoz, A., University of Alberta. Dept. of Civil and Environmental Engineering 2009. Enhanced Oil Recovery Modeling Using a Pressure Pulse-geomechanical Black Oil Simulator: University of Alberta.

[21] Spanos, T., Davidson, B., Dusseault, M.B. and Samaroo, M. 1999. Pressure Pulsing At the Reservoir Scale: A New IOR Approach. Presented at the Annual Technical Meeting, Jun 14 - 18, 1999 1999.

[22] Streeter, V.L., Wylie, E.B. and Bedford, K.W. 1998. Fluid mechanics: WCB/McGraw Hill.

[23] van der Grinten, J.G.M., van Dongen, M.E.H. and van der Kogel, H. 1987. Strain and pore pressure propagation in a watersaturated porous medium. Journal of Applied Physics 62 (12): 4682-7. doi: http://dx.doi.org/10.1063/1.339018.

[24] van der Grinten, J.G.M., van Dongen, M.E.H. and van der Kogel, H. 1985. A shocktube technique for studying porepressure propagation in a dry and watersaturated porous medium. Journal of Applied Physics 58 (8): 2937-42. doi: http://dx.doi.org/10.1063/1.335841.

[25] Verruijt, A. 2010. An introduction to soil dynamics [electronic resource]. Dordrecht; New York: Springer.

[26] Virieux, J. 1986. P-SV wave propagation in heterogeneous media: Velocitystress finitedifference method. Geophysics 51 (4): 889-901. Wang, X., Hovem, K.A., Moos, D. and Quan, Y. 2008. Water Hammer Effects on Water Injection Well Performance and Longevity. Presented at the SPE International Symposium and Exhibition on Formation Damage Control, 01/01/2008.

[27] Wilkins, M.L. 1980. Use of artificial viscosity in multidimensional fluid dynamic calculations. Journal of Computational Physics 36 (3): 281-303.

[28] Wisse, C.J. 1999. On Frequency Dependence of Acoustic Waves in Porous Cylinders: University of Technology.

Appendix A-Governing equations under axisymmetric cylindrical conditions

Under axisymmetric conditions one can write:

$$\frac{\partial}{\partial \theta} = 0, \sigma_{r\theta} = \sigma_{z\theta} = 0 \tag{A.1}$$

$$\epsilon_{rr} = \frac{\partial w_r}{\partial r}; \epsilon_{\theta\theta} = \frac{w_r}{r}; \epsilon_{zz} = \frac{\partial w_z}{\partial z} \tag{A.2}$$

We also have:

$$Div(\boldsymbol{w}) = \frac{\partial v}{\partial t} = \dot{\epsilon_{rr}} + \dot{\epsilon_{\theta\theta}} + \dot{\epsilon_{zz}} \tag{A.3}$$

Therefore the equations can be rewritten as:

$$\rho_f \frac{\partial v_r}{\partial t} = -\frac{\partial p}{\partial r} - n\frac{\mu}{k_r}(v_r - w_r) + \mu[\frac{\partial^2 v_r}{\partial r t^2} + \frac{1}{r}\frac{\partial v_r}{\partial r} + \frac{\partial^2 v_r}{\partial z^2}$$
$$-\frac{v_r}{r^2}] + (\mu + \lambda_f)[\frac{\partial^2 v_r}{\partial r^2} + \frac{1}{r}\frac{\partial v_r}{\partial r} - \frac{v_r}{r^2} + \frac{\partial^2 v_r}{\partial r \partial z}] + \frac{\rho_{12}}{n}\frac{\partial(v_r - w_r)}{\partial t} \tag{A.4}$$

$$\rho_f \frac{\partial v_z}{\partial t} = -\frac{\partial p}{\partial z} - n\frac{\mu}{k_z}(v_z - w_z) + \mu[\frac{\partial^2 v_z}{\partial r^2} + \frac{1}{r}\frac{\partial v_z}{\partial r} + \frac{\partial^2 v_z}{\partial z^2}$$
$$+(\mu + \lambda_f)[\frac{\partial^2 v_r}{\partial r \partial z} + \frac{1}{r}\frac{\partial v_r}{\partial z} + \frac{\partial^2 v_r}{\partial z^2}] + \rho_f g + \frac{\rho_{12}}{n}\frac{\partial(v_z - w_z)}{\partial t} \tag{A.5}$$

where $\lambda_f = -2\mu/3$ assuming shear stress in liquids are zero.

$$n\rho_f \frac{\partial v_r}{\partial t} + (1-n)\rho_s\frac{\partial w_r}{\partial t} = \frac{\partial \sigma'_{rr}}{\partial r} + \frac{\partial \sigma'_{rz}}{\partial z} + \alpha\frac{\partial p}{\partial r} + \frac{\sigma'_{rr} - \sigma'_{\theta\theta}}{r} - K_s\frac{\partial n}{\partial r}; \tag{A.6}$$

$$n\rho_f \frac{\partial v_z}{\partial t} + (1-n)\rho_s\frac{\partial w_z}{\partial t} = \frac{\partial \sigma_{rz}}{\partial r} + \frac{\partial \sigma'_{zz}}{\partial z} + \alpha\frac{\partial p}{\partial z} + \frac{\sigma_{rz}}{r} - K_s\frac{\partial n}{\partial z} + \rho g; \tag{A.7}$$

$$S_p\frac{\partial p}{\partial t} = -\alpha\frac{\partial \epsilon_v}{\partial t} - \frac{\partial[n(v_r - w_r)]}{\partial r} - \frac{\partial[n(v_z - w_z)]}{\partial z} = n\frac{(v_r - w_r)}{r} \tag{A.8}$$

$$\frac{dn}{dt} = (\alpha - n)[C_s\frac{dp}{dt} + \frac{\partial \epsilon_v}{\partial t}] \tag{A.9}$$

Appendix B-Solution method

To solve the equations, finite difference discretization is applied with second order approximation in space and first order backward approximation in time given by:

$$\frac{\partial f}{\partial x} = \frac{(f_{x+\Delta x} - f_{x-\Delta x})}{2\Delta x} + O(\Delta x^2), \tag{B.1}$$

$$\frac{\partial f}{\partial t} = \frac{(f^{t+\Delta t} - f^t)}{\Delta t} + O(\Delta t). \tag{B.2}$$

The explicit time marching scheme is used because of the complexity and nonlinearity of the equations. However, this method imposes conditional stability and small time step with fine mesh are required to achieve stable solutions.

To solve the equations, they are simplified and rearranged in the following order so that they can be solved sequentially.

$$\frac{\partial v_j}{\partial t} = \frac{-1}{\rho_f - \rho_{12}/n}(p_{,j} + \frac{n\mu}{k}(v_j - w_j) - (v_{j,ii} + \frac{1}{3}v_{i,ij}) + \frac{\rho_{12}}{n}\frac{\partial w_j}{\partial t}) \tag{B.3}$$

$$\frac{\partial w_i}{\partial t} = \frac{1}{\rho_s(1-n)}(-n\rho_f\frac{\partial \mathbf{v}_i}{\partial t} + \sigma_{ij,j} + \rho g_i - K_s n_{,i}) \tag{B.4}$$

$$\frac{dp}{dt} = \frac{-1}{S_p}(\alpha\mathbf{w}_{i,i} + (\mathbf{v}_i - \mathbf{w}_i).(nC_f p_{,i} + n_{,i}) + n(\mathbf{v}_i - \mathbf{w}_i)_{,i}) \tag{B.5}$$

$$\frac{dn}{dt} = (\alpha - n)C_s\frac{d\mathbf{p}}{dt} + (\alpha - n)\mathbf{w}_{i,i} \tag{B.6}$$

$$\dot{\epsilon}_{ij} = \frac{1}{2}(\mathbf{w}_{i,j} + \mathbf{w}_{j,i}) \tag{B.7}$$

$$\dot{\sigma'_{ij}} = (K_s - 2/3G)\dot{\epsilon}_{ij}\delta_{ij} + 2G\dot{\epsilon}_{ij} \tag{B.8}$$

First, fluid velocity is calculated explicitly from the fluid momentum balance. Then the new values for fluid velocities (shown in bold) are used in the momentum balance to find solid velocities. Calculated values of velocities for both phases are used in the mass balance equation to solve for pore pressure. Finally, using the new values of pore pressure and solid velocities, strains rates are calculated and porosity and stresses are updated. The algorithm is shown in Figure B1.
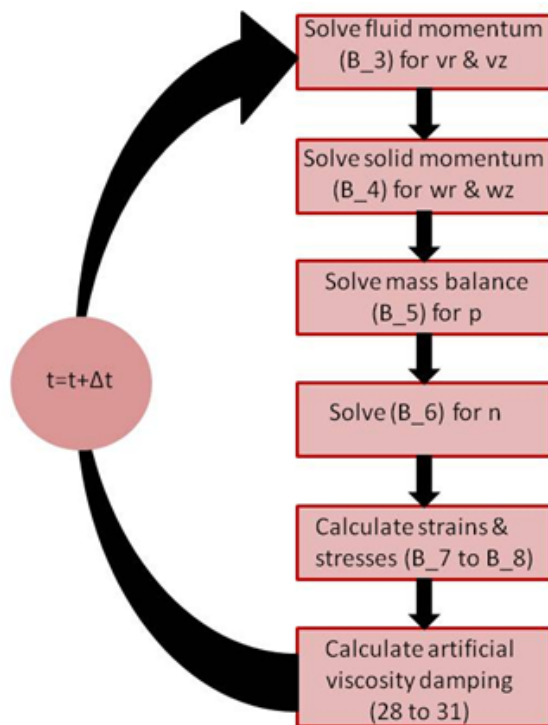
Figure B1: Algorithm used to solve the equations